Article

Performance Evaluation of GEDI for Monitoring Changes in Mountain Glacier Elevation: A Case Study in the Southeastern Tibetan Plateau

Zhijie Zhang [1], Yong Han [2], Liming Jiang [3], Shuanggen Jin [2,4], Guodong Chen [1,*] and Yadi Song [1]

1 School of Geography Science and Geomatics Engineering, Suzhou University of Science and Technology, Suzhou 215009, China; zjzhang@usts.edu.cn (Z.Z.)
2 School of Surveying and Land Information Engineering, Henan Polytechnic University, Jiaozuo 454000, China
3 State Key Laboratory of Precision Geodesy, Innovation Academy for Precision Measurement Science and Technology, Chinese Academy of Sciences, Wuhan 430077, China
4 Shanghai Astronomical Observatory, Chinese Academy of Sciences, Shanghai 200030, China
* Correspondence: cgd@usts.edu.cn

Abstract

Mountain glaciers are the most direct and sensitive indicators of climate change. In the context of global warming, monitoring changes in glacier elevation has become a crucial issue in modern cryosphere research. The Global Ecosystem Dynamics Investigation (GEDI) is a full-waveform laser altimeter with a multi-beam that provides unprecedented measurements of the Earth's surface. Many studies have investigated its applications in assessing the vertical structure of various forests. However, few studies have assessed GEDI's performance in detecting variations in glacier elevation in land ice in high-mountain Asia. To address this limitation, we selected the Southeastern Tibetan Plateau (SETP), one of the most sensitive areas to climate change, as a test area to assess the feasibility of using GEDI to monitor glacier elevation changes by comparing it with ICESat-2 ATL06 and the reference TanDEM-X DEM products. Moreover, this study further analyzes the influence of environmental factors (e.g., terrain slope and aspect, and altitude distribution) and glacier attributes (e.g., glacier area and debris cover) on changes in glacier elevation. The results show the following: (1) Compared to ICESat-2, in most cases, GEDI overestimated glacier thinning (i.e., elevation reduction) to some extent from 2019 to 2021, with an average overestimation value of about -0.29 m, while the annual average rate of elevation change was relatively close, at -0.70 ± 0.12 m/yr versus -0.62 ± 0.08 m/yr, respectively. (2) In terms of time, GEDI reflected glacier elevation changes at interannual and seasonal scales, and the trend of change was consistent with that found with ICESat-2. The results indicate that glacier accumulation mainly occurred in spring and winter, while the melting rate accelerated in summer and autumn. (3) GEDI effectively monitored and revealed the characteristics and patterns of glacier elevation changes with different terrain features, glacier area grades, etc.; however, as the slope increased, the accuracy of the reported changes in glacier elevation gradually decreased. Nonetheless, GEDI still provided reasonable estimates for changes in mountain glacier elevation. (4) The spatial distribution of GEDI footprints was uneven, directly affecting the accuracy of the monitoring results. Thus, to improve analyses of changes in glacier elevation, terrain factors should be comprehensively considered in further research. Overall, these promising results have the potential to be used as a basic dataset for further investigations of glacier mass and global climate change research.

1. Introduction

Glaciers, as an important component of the cryosphere, are extremely sensitive to climate change [1]; understanding their dynamic changes is therefore important for climate indications [2,3]. In the context of global warming, the glacier thinning rate has accelerated in recent decades [4–6]. This has an important impact on regional water resources, and causes varying degrees of glacier-related disasters [7–9]. Outside of the Antarctic and Arctic, HMA, including the Tibetan Plateau and its surrounding mountain ranges (the Himalayas, Karakoram, Tien Shan, and Pamir), features the highest concentrations of glaciers, making it a critical indicator of global climate change. Of these areas, glaciers in the Southeastern Tibetan Plateau (SETP) have been thinning significantly, at about three times the average rate of mass loss across the entire Tibetan Plateau region [10,11]. Therefore, the detection and monitoring of the present state and future changes in SETP glaciers are of great significance for understanding climate change directly and preventing glacier-related disasters.

Spaceborne remote sensing systems, including Digital Globe WorldView-1/2/3, GeoEye-1, and ASTER, have enabled the large-scale monitoring of polar and mountain glaciers, overcoming challenges associated with in situ measurements in inaccessible regions [12–14]. In 2018, NASA launched two complementary LiDAR missions—GEDI (Global Ecosystem Dynamics Investigation) and ICESat-2—to advance their Earth observation capabilities [15]. While ICESat-2 focuses on ice sheet and glacier mass balance [16], GEDI was designed primarily for forest canopy and carbon storage assessment [17]. Nevertheless, both missions provide valuable elevation data for global topographic mapping.

GEDI, mounted on the International Space Station, collects high-resolution elevation measurements between 51.6°N and 51.6°S [18,19]. Studies have demonstrated its accuracy in forest structure mapping [19], estimations of biomass [20], and assessments of species richness [21]. For example, Adam et al. [22] assessed the accuracy of GEDI terrain elevation and canopy height estimates in European temperate forests, showing that, when excluding steep slope areas, the GEDI ground elevation estimates showed a consistently high accuracy under most conditions. Kutchartt et al. [23] assessed the GEDI LiDAR over steep topography, suggesting that terrain slope was the most serious factor affecting accuracy, likely linked to the uncertainty of footprint geolocation. Quiros et al. [24] evaluated GEDI elevation accuracy by comparing the ground elevation differences derived from its measurements with those obtained with airborne laser scanning LiDAR- and TanDEM-X-derived DEMs in southwest Spain. Generally, their results showed that GEDI could achieve better agreement with the LiDAR data and that there was a clear relation between the errors and the slope: the greater the slope, the greater the errors (RMSE). Hamoudzadeh et al. [25] assessed the accuracy of GEDI data in monitoring the elevation of the Rutor and Belvedere glaciers in northern Italy using reference-level measurements from UAV DEMs, in which they focused on detecting and eliminating outliers.

However, its performance degrades in steep terrain due to geolocation uncertainties. Limited validation in glacial environments—such as preliminary assessments in the European Alps (requiring rigorous outlier filtering) [25]—suggests promise, but highlights the need for further evaluation, particularly in rugged mountain regions where glacier dynamics are most pronounced.

ICESat-2 is equipped with a photon-counting laser altimeter, ATLAS (Advanced Topographic Laser Altimeter System). It emits green (532 nm) laser pulses every 0.7 m along the track with a frequency of 10 kHz. Compared with its predecessor full-waveform laser altimeter ICESat (2003–2009), ICESat-2 provides much denser observational coverage and obtains more accurate estimates of ice mass balance, the elevation of ice sheets, and measurements of glaciers, sea ice, and snow depth [26–28]. Using DEM differencing, Zhao et al. [11] combined ICESat-2 with ICESat, CryoSat-2 altimetric data, and GRACE gravity data to explore glacier mass balance across the SETP. The results demonstrate that there was rapid and heterogeneous glacier ablation with a mean mass loss rate of 0.66 ± 0.02 m water equivalent (w.e.)/a during 2003–2020. Based on ICESat-2 ATL06 and NASADEM, Fan et al. [29] estimated glacier mass balance over HMA during 2000–2021, which demonstrated that HMA experienced a significant mass loss at a rate of −0.18 ± 0.12 m w.e./a. Utilizing ICESat-2 observations, Wang and Sun [30] demonstrated distinct seasonal patterns in HMA glacier surface elevation, with peak thicknesses occurring earliest in westerly dominated regions (February), followed by Indian monsoon areas (May) and transitional zones (June). Similarly, Shen, Jia, and Ren [31] analyzed the inter- and intra-annual glacier elevation change detected by ICESat-1&2 data in 2003–2020, indicating that glacier elevation change in HMA had large spatial heterogeneity, with the reduction mainly occurring in the marginal region.

In addition, more studies of changes in glacier elevation over HMA found that ATL06 had a higher accuracy than other DEM products [32,33]. The ATL06 product has a height accuracy above 5 cm in the Antarctic [34] and surface measurement precision above 20 cm in Qilian Shan [35]. Consequently, these studies have shown that ATL06 is feasible as a reference to assess the performance of GEDI when monitoring glacier elevation variations.

To assess the performance of both ICESat-2 and GEDI, Liu, Cheng, and Chen [36] used high-resolution, locally calibrated airborne LiDAR products to test the GEDI L2A and ICESat-2 ATL08 products at 40 sites located in the U.S. mainland, Alaska, and Hawaii that contained various ecoclimatic areas and vegetation types. The results show that GEDI and ICESat-2 can yield reasonable estimates of terrain height, with root mean squared errors of 2.24 and 4.03 m for mid and low latitudes, respectively, and 0.98 m for high latitudes (ICESat-2 only). Generally, ICESat-2 outperformed GEDI when retrieving terrain height, but both had better accuracy than the existing SRTM and GMTED DEM products. Urbazaev et al. [37] investigated the accuracy of both sensors in four different land cover classes and six forest types located in Brazil, Germany, South Africa, and the USA. The results indicate that both missions provided accurate terrain elevation estimates across different land cover classes and forest types, with a mean error of less than 1 m, except in tropical forests. However, terrain slope strongly impacted the accuracy of both the ICESat-2 and GEDI terrain elevation estimates.

The objective of this study is to assess the performance of the GEDI L2A product when estimating changes in mountain glacier elevation by comparing a counterpart derived from ICESat-2, improving our understanding of GEDI terrain height products when applied to mountain glaciers.

2. Study Area and Datasets

2.1. Study Area

The study area (27.95°N–31.53°N, 92.10°E–98.32°E) encompasses the eastern Nyainqentanglha and Himalayan Ranges, western Hengduan Mountains, and the Parlung Zangbo River Basin (Figure 1). This high-relief terrain (mean elevation > 4000 m) features extreme vertical contrasts, from the 7782 m peak of Namcha Barwa to sub-500 m valleys, with dense river networks including the Yarlung Zangbo, Nu, and Lancang

Rivers [38].The study area features a subtropical monsoon climate dominated by South Asian monsoon systems, where warm, humid Indian Ocean air masses collide with the Tibetan Plateau's eastern mountain ranges, generating orographic precipitation. This creates the Plateau's wettest zone (2500–3000 mm annual rainfall), with prolonged monsoon seasons (March–October) [39]. In the glacier regions (such as the eastern Nyainqêntanglha Mountains and the Kangri Garpo Range), the annual average temperature typically ranges between −5 °C and 6 °C, varying with altitude [40], combining heavy precipitation with relatively mild temperatures to form China's primary center for monsoon-fed maritime glaciers.
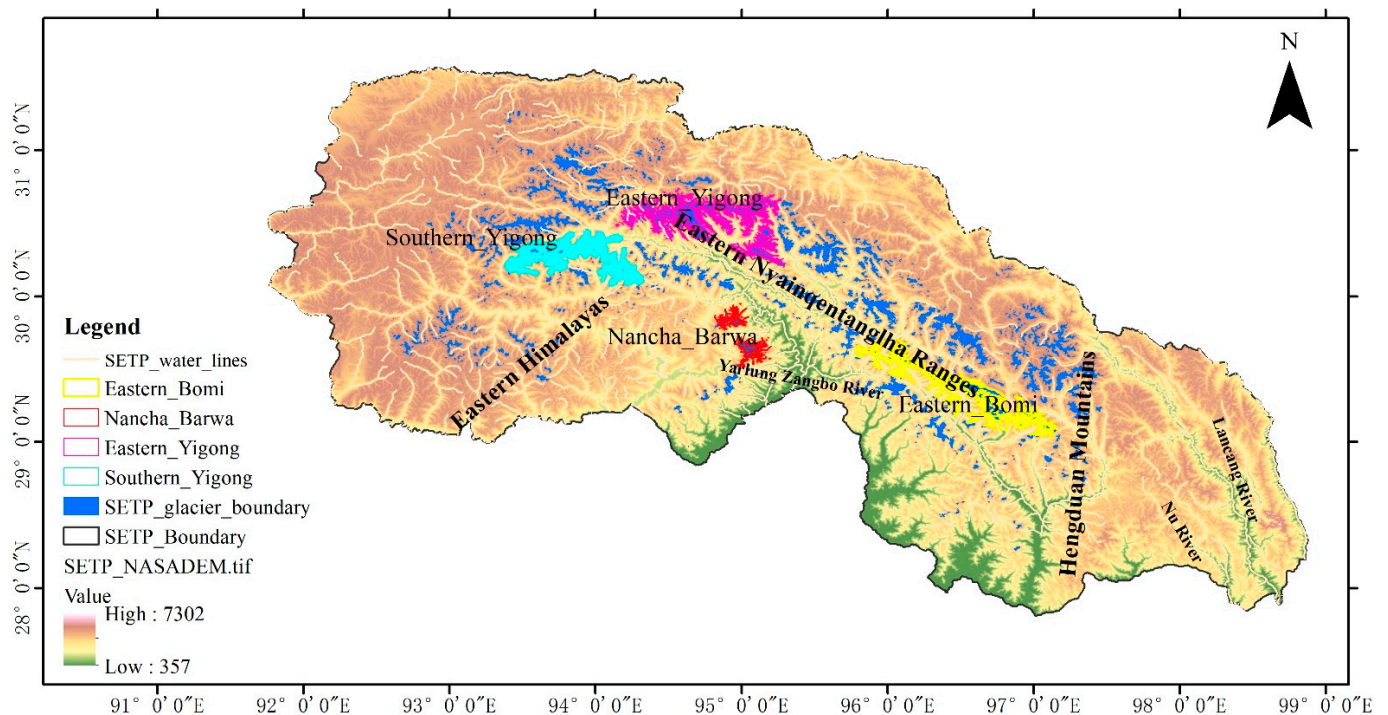

Figure 1. Location of the SETP, and the distribution of glacier boundaries within it. The dark line delineates the boundaries of the SETP (the background elevation is marked by NASADEM, downloaded from https://www.earthdata.nasa.gov/data/catalog/lpcloud-nasadem-hgt-001, accessed on 5 May 2024), and blue polygons denote glacier outlines from the above glacier inventory. The colors mark the four sub-regions where the most glaciers are concentrated.

2.2. Datasets

This study employs three primary data sources: GEDI/ICESat-2 altimetry data, TanDEM-X reference DEM, and glacier inventory attributes (see Table 1 for specifications).

Table 1. Detailed information on the main data used in this study.

Description	Data	Time Span	Spatial Resolution	Temporal Resolution	Data Sources
Satellite altimetry	GEDI L2A	April/2019–July/2021	25	Monthly	https://www.earthdata.nasa.gov/data/catalog/lpcloud-gedi02-a-002 (accessed on 10 May 2024)
	ICESat-2 ATL06	April/2019–July/2021	20	91d	https://nsidc.org/data/atl06/versions/5 (accessed on 10 May 2024)
Ancillary datasets	TanDEM-X	2010–2015	90	*	https://download.geoservice.dlr.de/TDM90/ (accessed on 8 January 2024)
	Glacier inventory	2007–2011	*	*	http://www.sciencedb.cn/dataSet/handle/376 (accessed on 4 May 2023)

* Denotes that this attribute is not applicable to the data.

2.2.1. GEDI L2A

The GEDI data products are organized in a four-level hierarchy: L1 provides geolocated waveform data; L2 (used in this study) delivers ground elevation and canopy metrics at 25 m resolution, referenced to the WGS-84 ellipsoid and including relative height metrics with TanDEM-X/SRTM reference elevations; L3 offers gridded canopy parameters; and L4 contains aboveground carbon estimates. This study employs NASA's GEDI L2A Version 2 dataset (updated April 2021), obtained from the Land Processes Distributed Active Archive Center (LPDAAC), for the period between April 2019 and July 2021. Our analysis focuses on SETP, utilizing a total of 1210 valid orbital datasets to examine three-dimensional surface characteristics. The dataset is publicly accessible through NASA's LPDAAC (https://www.earthdata.nasa.gov/data/catalog/lpcloud-gedi02-a-002 (accessed on 10 May 2024)).

2.2.2. ICESat-2 ATL06

ICESat-2/ATLAS, featuring enhanced spatial resolution using six laser beams that provide precise elevation measurements without penetration effects. This study uses Level 3A ATL06 Version 5 data (Land Ice Height). The dataset, available from NASA Earthdata (https://earthdata.nasa.gov/), delivers 40 m segment heights (WGS-84 ellipsoid) with 20 m along-track spacing, incorporating first-photon bias correction and comprehensive quality assessment parameters. To maintain seasonal consistency and minimize temporal biases in our comparative analysis with GEDI data, we specifically selected 528 ICESat-2 datasets, corresponding with matching observation periods. This approach ensures robust cross-validation between the two altimetry datasets, while accounting for potential seasonal variations in surface characteristics.

2.3. Auxiliary Data

2.3.1. Glacier Inventory

The glacier dataset used in this study was extracted by Ke et al. [39]. We selected the glacier inventory due to its demonstrated superior performance in the SETP, particularly in (1) combining multi-sensor (Landsat + PALSAR) data to overcome cloud contamination, (2) employing advanced machine learning classification (94.2% accuracy), and (3) better detecting small (<0.05 km^2) and debris-covered glaciers compared to global inventories (RGI/GLIMS). This study analyzed 7182 glaciers (6440.97 km^2 total area) using vector boundary files containing key attributes (area, elevation range, slope, etc.). Glacier footprints from the GEDI, ICESat-2, and DEM datasets were classified accordingly. To assess spatial variability in elevation changes, four high-density subregions (Eastern/Southern Yigong, Nancha Barwa, Eastern Bomi) were prioritized, following Zhao et al. [11]'s framework.

2.3.2. TanDEM-X Data

This study employed the 90 m-resolution TanDEM-X Digital Elevation Model (DEM), publicly released in 2018 by the German Aerospace Center (DLR), as reference elevation data. The dataset originates from the high-resolution (12 m) global DEM acquired between 2010 and 2015 through interferometric synthetic aperture radar (InSAR) measurements by the twin-satellite TerraSAR-X/TanDEM-X mission [40]. While the original 12 m product demonstrated excellent vertical accuracy (3.49 m absolute error when validated against ICESat data) [31,41], we utilized its resampled 90 m version to ensure data accessibility and processing efficiency. This DEM product represents glacier surface elevations as of January 2015, although it should be noted that, being an unedited version, it may contain minor artifacts due to the absence of gap-filling procedures [42,43]. The dataset was obtained

from the DLR Geoservice portal (https://download.geoservice.dlr.de/TDM90/, accessed on 8 January 2024) and served as our baseline for elevation change detection in this study.

3. Methods

This section contains outlines of the preprocessing of the GEDI and ICESat-2 footprints and the elevation extraction, a comparison of the elevation change results, and the metrics for glacier elevation changes.

3.1. Data Preprocessing

GEDI is a full-waveform LiDAR system that utilizes three synchronized lasers—one split into two "coverage beams" and two full-power beams—which collectively generate eight parallel ground tracks (~600 m spacing) within a 4.2 km swath through beam dithering operating at 242 Hz. According to the principle of GEDI positioning, the location of the ground return within a waveform is determined using the position of the last detected peak; thus, the parameter 'elev_lowestmode' of each beam was extracted to represent glacier surface elevation. In our study, the default terrain elevation estimates that vary among the products' six algorithms depending on plant functional type [44] were selected for testing, and different beam modes (power or coverage) were not distinguished. Furthermore, 'lon_lowestmode' and 'lat_lowestmode', which determine the latitude and longitude information of each surface footprint, were also adopted. In addition, the quality-controlled footprints (quality_flag = 1, degrade_flag = 0) were used to filter erroneous and lower-quality returns.

In terms of ATL06 preprocessing, the extracted fields contained geolocation 'latitude, longitude', surface elevation 'h_li', elevation uncertainty standard error 'sigma_geo_h', and quality measures 'atl06_quality_summary' for each segment. Like GEDI, we did not distinguish strong and weak beam modes for terrain estimation. Of these, we used the 'atl06_quality_summary' parameter to obtain reliable high-quality data; when scored with '0', this implies that no data-quality problem was found within the segment. The parameter 'sigma_geo_h' is a comprehensive indicator of total vertical geolocation error due to precise orbit determination and precise point determination, including the effects of the horizontal geolocation error on the segment vertical error; values less than or equal to 25 m within the glacier inventory were selected to derive reliable reference data for GEDI.

3.2. Glacial Elevation Change Extraction

To estimate glacier elevation changes, the height measurements from GEDI and ICESAT-2 were compared against the reference TanDEM-X DEM, which contains information on past glacier elevations. The detailed procedures are as follows:

(1) Initial extraction of GEDI L2A and ICESat-2 ATL06 footprints within SETP glacier boundaries were performed. (2) Glacier elevations, geolocations, and quality flags were then extracted, with raw data filtered using quality flags (GEDI: quality_flag = 1, degrade_flag = 0; ICESat-2: atl06_quality_summary = 0, sigma_geo_h $\leq$ 25). (3) TanDEM-X 90 m elevation values were bilinearly interpolated to each footprint location, leveraging the shared WGS84 ellipsoid reference system to avoid height conversions. (4) Robust outlier removal excluded elevation changes (Δh) exceeding a $\pm$ 50 m threshold. (5) Cumulative glacier elevation changes were derived by averaging all valid footprints. (6) Finally, annualized change rates were calculated by normalizing multi-year cumulative changes, enabling the quantification of glacier thinning dynamics. Figure 2 presents the specific implementation steps of this approach.
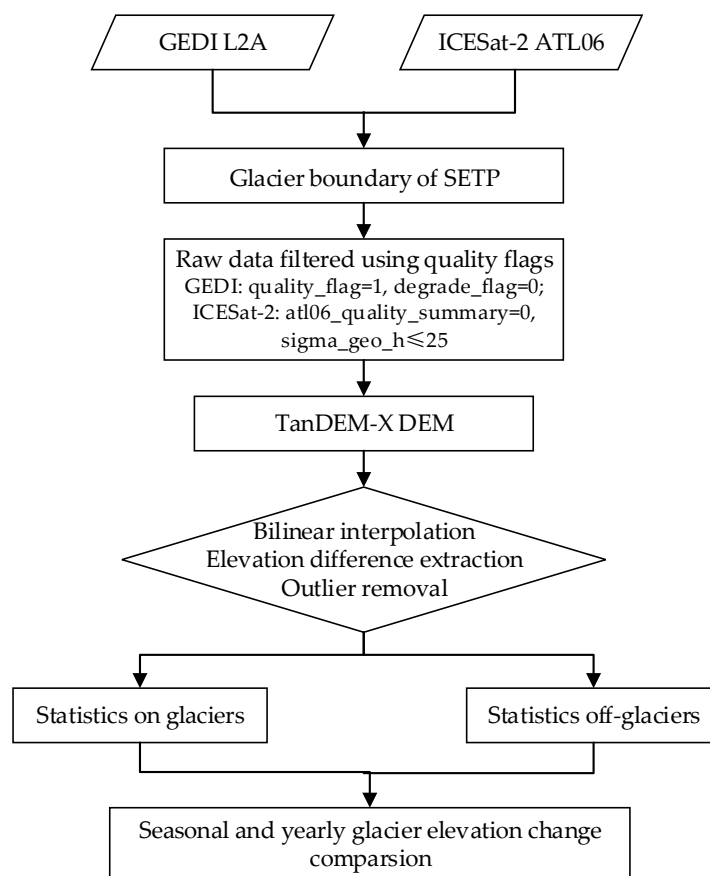
Figure 2. Methodological flowchart.

3.3. Statistical Analysis

To evaluate the elevation change estimated using GEDI, the statistics of cumulative variations, mean annual elevation change rate, and seasonal variability distributed over the entire SETP and the four major sub-regions where most glaciers were gathered were compared with corresponding alternatives derived from ICESat-2. Meanwhile, the statistics from the off-glacier area were tabulated to analyze the possible uncertainty of each mission. The cumulative changes over multiple years in glacier elevation were estimated by calculating the mean of all effective laser footprints.

$$\Delta h = \frac{\sum \Delta h_{GEDI} / \Delta h_{ICESat\text{-}2}}{n} \tag{1}$$

where Δh represents the accumulated elevation change over the years; $\sum \Delta h_{GEDI} / \Delta h_{ICESat\text{-}2}$ are the overall elevation variations in effective GEDI L or ICESat-2 footprints; and n is the corresponding footprints of GEDI or ICESat-2.

Calculating the annual average change can reflect the rate of glacier elevation change. The expression for calculating the rate of glacier elevation change is shown in the following equation:

$$v = \frac{\Delta h}{T_{GEDI/ICESat\text{-}2} - T_{TanDEM\text{-}X}} \tag{2}$$

where v represents the rate of elevation change; $T_{GEDI/ICESat\text{-}2}$ is the data collection time of GEDI L2A or ICESat-2; and $T_{TanDEM\text{-}X}$ is the data product acquisition time of TanDEM-X 90 m.

To statistically analyze the cumulative elevation changes and annual elevation change rates, we employed both mean and median values as central tendency measures, along with

standard deviation (SD) and median absolute deviation (MAD) as indicators of variability and error ranges. The MAD was estimated as follows:

$$SD = \sqrt{\frac{1}{n}\sum\nolimits_{i=1}^{n}\left(\Delta h_i - \mu\right)^2} \tag{3}$$

$$MAD = median\left(|\Delta h_i - m(\Delta h)|\right) \tag{4}$$

where Δh_i corresponds to the height change of the *i*th footprint and μ and *m*Δ*h* are the mean and median of all the individual height differences.

4. Results and Analysis

4.1. Glacier Elevation Change Retrieved Using GEDI Versus ICESat-2

4.1.1. Changes in Statistics of the Overall SETP

Based on the above data preprocessing, the proportion of retained GEDI samples from 2019 to 2021 was 22.93%, 32.10%, and 32.49%, respectively, with an average effective data rate of 29.17% for elevation change monitoring. Figure 2 shows histograms of the height changes derived from GEDI versus ICESat-2 in 2019 in the glacier and off-glacier regions. It can be seen that the number of ICESat-2 points exceeded that of GEDI in the glacier area. The denser footprints indicate that using ICESat-2 to evaluate GEDI is a feasible approach. Compared to ICESat-2, in the glacier area, GEDI presented a similar distribution of positive and negative changes to that of ICESat-2, which were biased towards the left (Figure 3a), indicating the elevation thinning of the glaciers. Outside glacier areas, GEDI exhibited a more asymmetric negatively skewed distribution. In addition to the larger dispersion of the GEDI data, larger height differences occurred relatively more commonly, as shown by the long tails of the histogram (Figure 3b). Theoretically, the elevation should remain constant in the off-glacier areas. However, this exception may be caused by seasonal variations (like snow cover), the quality of multi-source data, and errors caused by interpolation processing.

Table 2 lists the cumulative elevation changes from 2019 to 2021 in glacier and off-glacier areas relative to the reference TanDEM-X in 2015. In terms of the numerical values, the changes retrieved from GEDI and ICESat-2 inside and outside the glaciers were negative, indicating the melting of glaciers and the lowering of the terrain in the off-glacier area, consistent with the long negative tail of elevation changes shown in Figure 2. Compared to ICESat-2, the glacier thinning values given by GEDI were larger than those of ICESat-2, no matter the mean or median metrics, indicating that GEDI overestimated this to some extent. Using the changes in GEDI minus those of ICESat-2, the differences in the means were −0.53 m, 0.30 m, and −0.64 m from 2019 to 2021, with an average difference of −0.29 m; the corresponding differences in the medians were −0.86 m, 0.27 m, and −0.83 m, with an average of −0.47 m. From the perspective of SD and MAD, the GEDI indicators were larger, but comparable to those of ICESat-2, with average differences of 0.54 m and 0.43 m in glacier areas, indicating the relatively discrete nature of the monitored glacier elevation variations. However, the 2020 data shows a notable discrepancy between GEDI (minimal change) and ICESat-2 (a ~1.2 m change); the differences likely arise from their distinct sensor characteristics (e.g., waveform vs. photon-counting lidar), varying spatiotemporal sampling (orbital patterns and seasonal coverage), and differences in data processing algorithms (e.g., noise filtering and ground detection).
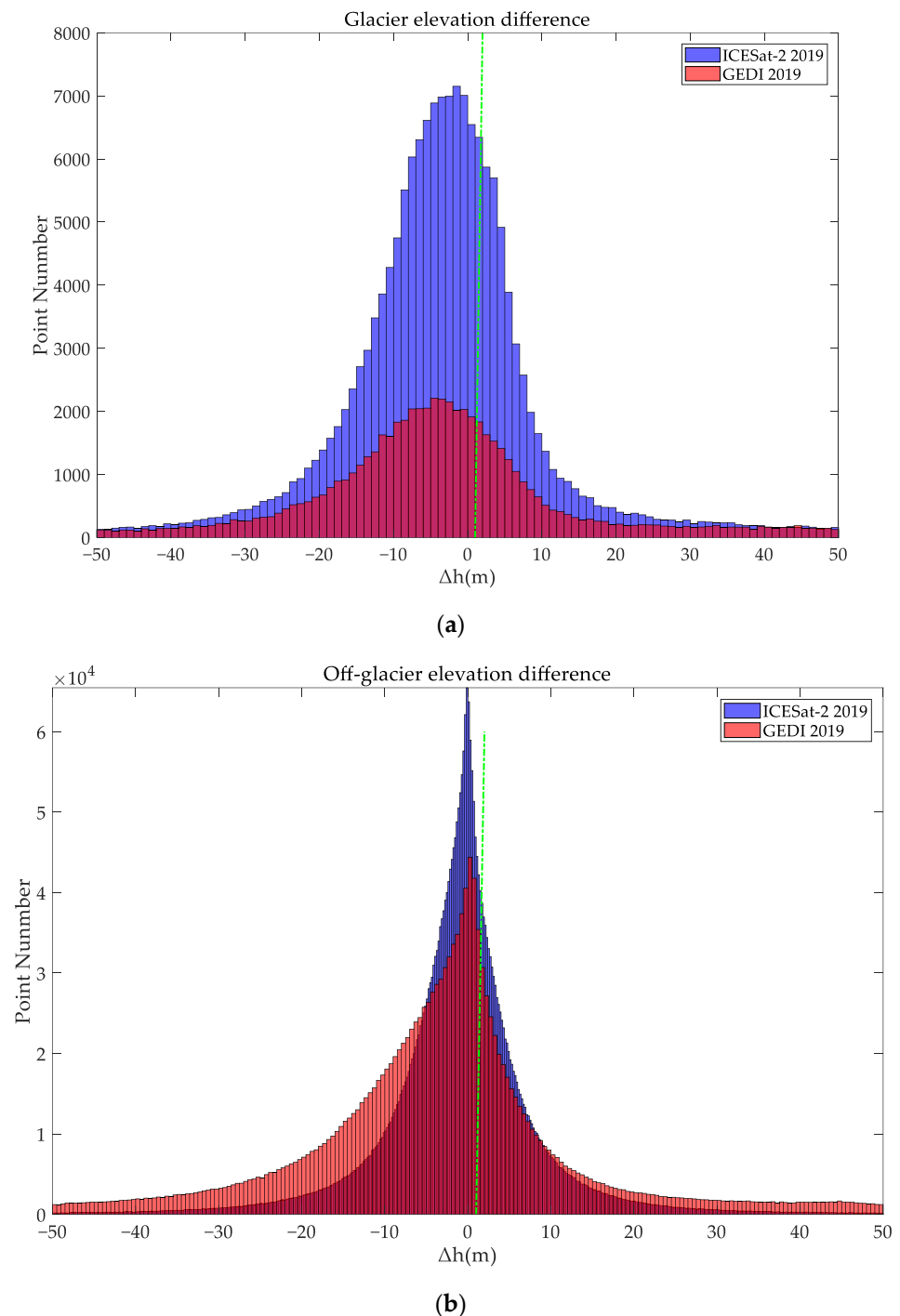
(**a**)

(**b**)

Figure 3. Comparison of height difference derived from GEDI and ICESat-2 (the green dashed line is the 0 axis): (**a**) glacier region; (**b**) off-glacier region.

For the off-glacier area, the means of GEDI and ICESat-2 were numerically close in 2019. However, the results of 2020 and 2021 show significant differences, at -0.94 m versus -0.56 m and -1.07 m versus -0.69 m, respectively, which indicates that the errors of GEDI were relatively larger and that it had, to some extent, overestimated the degree of decline in terrain altitude. However, from the perspective of the median, the values of all three years were closer, indicating that using the median of GEDI to represent terrain altitude changes may be more robust. Meanwhile, the SD and MAD indicators also revealed that the GEDI data were relatively scattered compared to ICESat-2. A possible explanation for this could be the much larger area that each GEDI footprint represents within a diameter of

approximately 25 m, which could lead to a moderately large height difference within the mountain terrain.

Table 2. Comparison of cumulative glacier elevation changes in glacier and off-glacier areas derived from GEDI and ICESat-2 from 2019 to 2021, with reference to TanDEM-X data in 2015.

	Glacier Area						Off-Glacier Area					
	GEDI			ICESat-2			GEDI			ICESat-2		
Statistics (m)	2019	2020	2021	2019	2020	2021	2019	2020	2021	2019	2020	2021
Mean	−3.36	−3.39	−4.6	−2.83	−3.69	−3.96	−0.76	−0.94	−1.07	−0.74	−0.56	−0.69
Median	−3.72	−3.74	−5.24	−2.86	−4.01	−4.41	−0.45	−0.61	−0.76	−0.56	−0.43	−0.54
SD	8.54	8.72	8.77	7.83	8.2	8.37	9.62	9.64	9.53	6.57	6.3	6.36
MAD	5.96	6.27	6.34	5.31	5.92	6.03	6.82	6.83	6.67	3.52	3.27	3.34

The annual average elevation change rate from 2019 to 2021 in the glacier and off-glacier outlines is tabulated in Table 3. The change rates of GEDI and ICESat-2 in the glacier areas were relatively close, with means of −0.60 ± 0.19 m/yr versus −0.58 ± 0.15 m/yr, and medians of −0.70 ± 0.12 m/yr versus −0.62 ± 0.08 m/yr, respectively. For the off-glacier area, the average change rates of terrain elevation were −0.15 ± 0.23 m/yr versus −0.11 ± 0.17 m/yr (mean) and −0.10 ± 0.17 m/yr versus −0.09 ± 0.09 m/yr (median). Taking into account the natural undulation of terrain and landforms, changes in snow thickness, and the working mechanism of laser altimeters, the elevation variations in the glacier-free areas were reasonable, and the numerical difference between GEDI and ICESat-2 was not significant. These results indicate that the GEDI products were reliable data sources for monitoring glacier elevation changes in mountain areas.

Table 3. Comparison of the annual elevation change rates of GEDI vs. ICESat-2 within and outside glacier areas.

	Glacier Area		Off-Glacier Area	
Statistics (m/yr)	Mean	Median	Mean	Median
GEDI	−0.60 ± 0.19	−0.70 ± 0.12	−0.15 ± 0.23	−0.10 ± 0.17
ICESat−2	−0.58 ± 0.15	−0.62 ± 0.08	−0.11 ± 0.17	−0.09 ± 0.09

4.1.2. Seasonal Change Comparison

Considering that the SETP region is significantly influenced by the Indian Ocean monsoon, which carries abundant warm and humid air flow that results in significant precipitation from June to September every year, we further evaluated and analyzed the monitoring capability of GEDI from the perspective of seasonal change. The four seasons are defined as follows: spring (from March to May), summer (from June to August), autumn (from September to November), and winter (from December to the next February), which are abbreviated as Spr. (Spring), Sum. (Summer), Aut. (Autumn), and Win. (Winter). Figure 4 illustrates the mean and the differences in elevation variations retrieved by GEDI and ICESat-2 from 2019 to 2021. As the test data of 2021 spanned from January to July, the changes in autumn were not reflected in 2021.
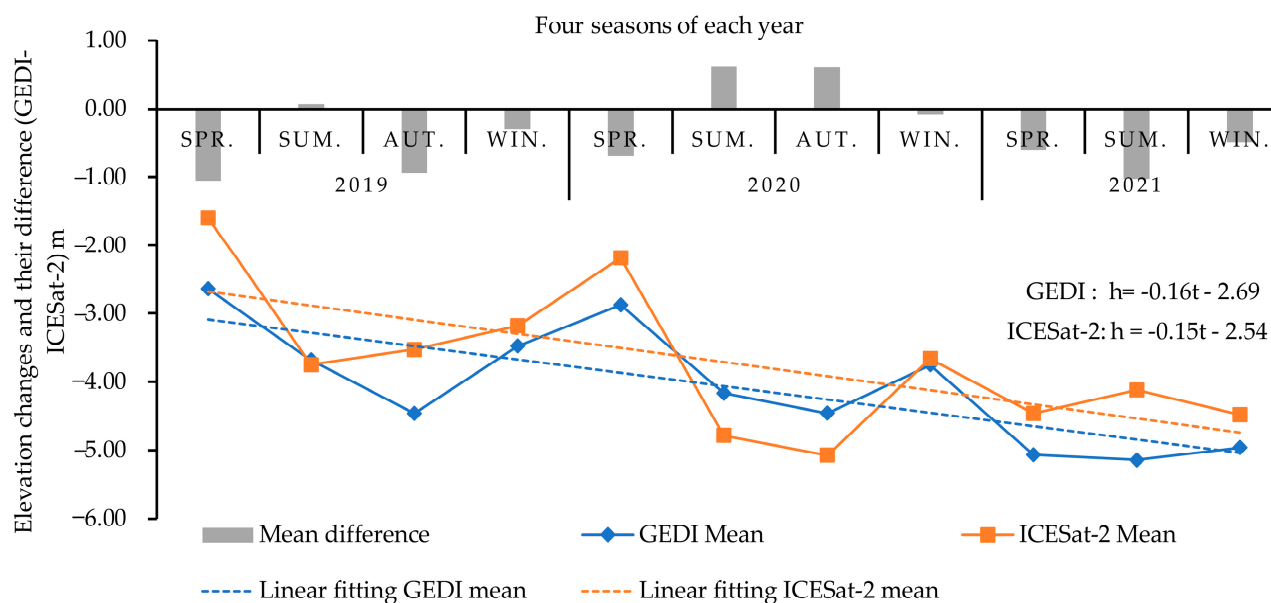
Figure 4. Seasonal comparison of glacier elevation variations derived from GEDI and ICESat-2 for the time period from 2019 to 2021. Here, the abbreviations (Spr.), (Sum.), (Aut.), (Win.) represent Spring, Summer, Autumn, and Winter, respectively. In the linear fitting formula, 't' represents time and 'h' denotes the thinning rate of glacier elevation change.

Generally, the trend of glacier elevation changes in different seasons identified by GEDI was similar to ICESat-2. From spring to winter, glacier melting gradually increased and then decreased. The smallest change occurred in spring, followed by winter, and the largest changes occurred in autumn, followed by summer. The average thinning identified by the two missions across the four seasons (spring, summer, autumn, and winter in sequence) were −3.19 m versus −2.69 m, −3.71 m versus −3.85 m, −4.03 m versus −4.13 m, and −3.72 m versus −3.44 m, respectively. Overall, GEDI showed a slight overestimation of the thinning rate of glacier elevation in different seasons, as reflected by the trends in the least squares regression model. The differences (GEDI minus ICESat-2) were within a ± 0.8 m range, as illustrated by the green bars. The maximum difference occurred in autumn, with an average absolute amount of 0.71 m, and the minimum difference occurred in winter, with an average absolute amount of 0.29 m. The values for spring and summer were approximately within 0.5 m. Nonetheless, GEDI reflected that the seasonal glacier elevation changes conformed to the accumulation patterns of oceanic glaciers in the SETP; for example, snow accumulation in spring and precipitation supply in summer provide ice mass replenishment, causing the corresponding elevation variation to decline slowly.

4.1.3. Change Statistics of Sub-Regions

In addition to temporal differences, we also considered possible heterogeneity in space. Therefore, we further analyzed the changes in the four sub-regions (Southern_Yigong, Eastern_Yigong, Nancha_Barwa, and Eastern_Bomi) with the highest concentrations of glaciers. Figure 5 shows the glacier elevation changes retrieved from GEDI and ICESat-2. Generally, both missions reflected that Southern_Yigong and Nancha_Barwa showed smaller levels of glacier melting. Their annual average thinning rates were −0.38 ± 0.08 m/yr versus −0.30 ± 0.05 m/yr, and −0.42 ± 0.10 m/yr versus −0.46 ± 0.03 m/yr, respectively. The other two sub-regions, Eastern_Yigong and Eastern_Bomi, showed larger changes: −0.58 ± 0.08 m/yr versus −0.50 ± 0.04 m/yr and −0.67 ± 0.22 m/yr versus −0.53 ± 0.10 m/yr, respectively. Of the four sub-regions, Eastern_Bomi and Southern_Yigong, respectively, showed the largest and lowest rates of elevation thinning. Inter-

estingly, the average elevation melting rate of Eastern_Yigong was very close to the mean elevation changes in the entire SETP (GEDI with −0.60 ± 0.19 m/yr versus ICESat-2 with −0.58 ± 0.15 m/yr). From a single regional perspective, GEDI reflected larger differences in the amounts and change trends compared to ICESat-2, especially in 2021, which may be caused by the quality of the GEDI data itself, terrain factors, and the uneven distribution of the two missions' data in each sub-region.
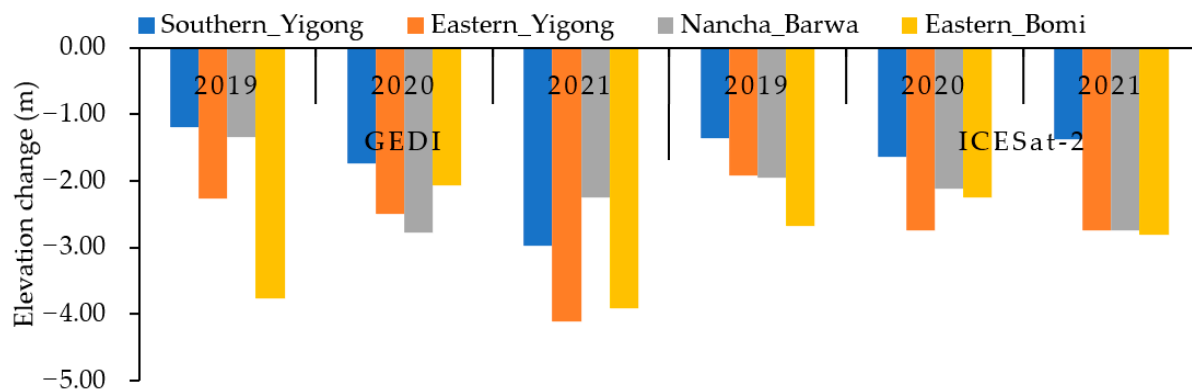

Figure 5. Mean of glacier elevation changes in the four sub-regions where glaciers gathered over the SETP.

4.2. Influence of Terrain Factors on Glacier Elevation Change

4.2.1. Terrain Elevation

To assess altitude-dependent glacier elevation changes, we classified elevations into 500 m intervals (Figure 6a). Glaciers were predominantly distributed between 4500 and 6000 m (97.96% by number, 96.32% by area), with peak concentrations at 5000–5500 m (57.89% of total). Both GEDI and ICESat-2 footprints aligned with this distribution, showing minimal coverage above 6000 m or below 4500 m.

To reduce the error caused by the small distribution of footprints within the low-altitude and high-altitude groups, we further analyzed the elevation change patterns of glaciers that were mainly distributed between elevations of 4500–6000 m at intervals of 300 m (Figure 6b), which revealed a clear altitudinal trend: maximum thinning occurred at lower elevations (4500–4800 m), likely due to smaller glacier areas, with diminishing thinning rates up to 5700 m. Above 5700 m, glaciers transitioned to accumulation. This pattern highlights the critical role of altitude in modulating glacier mass balance, with lower-elevation glaciers exhibiting greater climate sensitivity.

Compared to ICESat-2, generally, GEDI overestimated the overall glacier elevation changes at different altitudes (Figure 6c). The cumulative elevation changes shown by GEDI for the five altitude levels were −6.43 m, −5.36 m, −4.94 m, −1.43 m, and 2.06 m, while the corresponding changes for ICESat-2 were −5.50 m, −3.97 m, −4.45 m, −0.64 m, and 4.12 m, respectively. At different altitude ranges, the differences between the two missions showed a trend of first increasing, then decreasing, and then increasing again. Among them, the minimum difference was about 0.5 m at altitudes of 5100–5400 m, and the maximum range was nearly 2 m at altitudes of 5700–6000 m. Overall, the magnitude of glacier thinning at different altitudes was influenced by the size and number of distributed glaciers and the number of effective footprints.
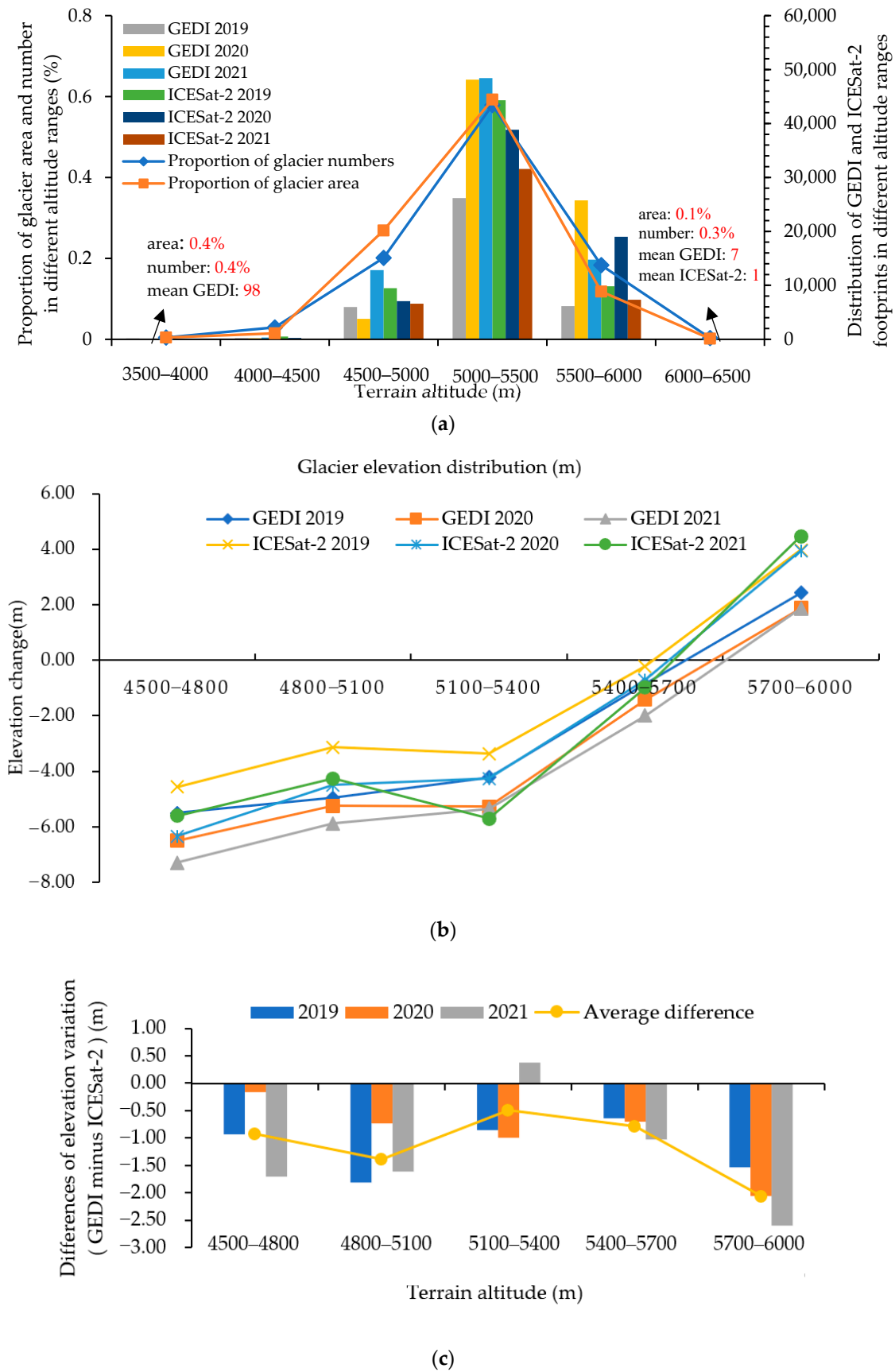
Figure 6. (**a**) Distribution of the number and area of glaciers with different mean slopes; (**b**) cumulative changes in glacier elevation within different terrain altitudes derived from GEDI and ICESat-2; (**c**) comparative analysis of elevation differences between GEDI and ICESat-2 at different altitudes.

4.2.2. Slope and Aspect

(1) Terrain slope and Glacier elevation changes

Slope, derived from glacier attribute data as surface-averaged values, significantly influences glacier morphology and mass balance. Categorized into five 10° intervals (from 5–15° to ≥45°), analysis revealed a bell-curve distribution peaking at 15–25° slopes (Figure 7a). This range contained 54.86% of total glacier area and 47.05% of glacier count. Conversely, steep slopes (>35°) represented only 4.98% of area and 14.33% of glaciers. To enable comprehensive slope-dependent studies, we retained all slope ranges using a GEDI footprint analysis without filtering.

(**a**)

(**b**)
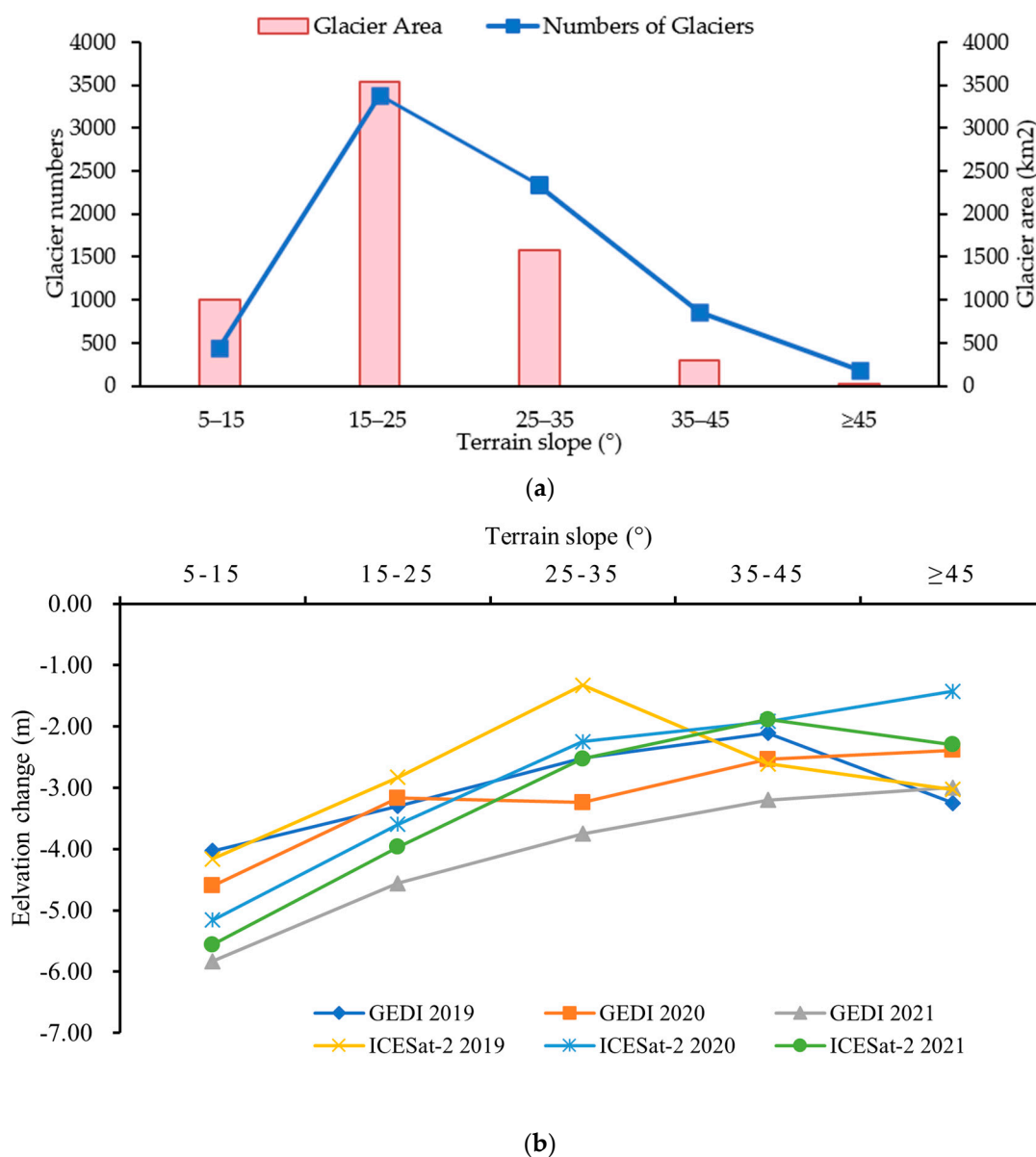
Figure 7. *Cont.*
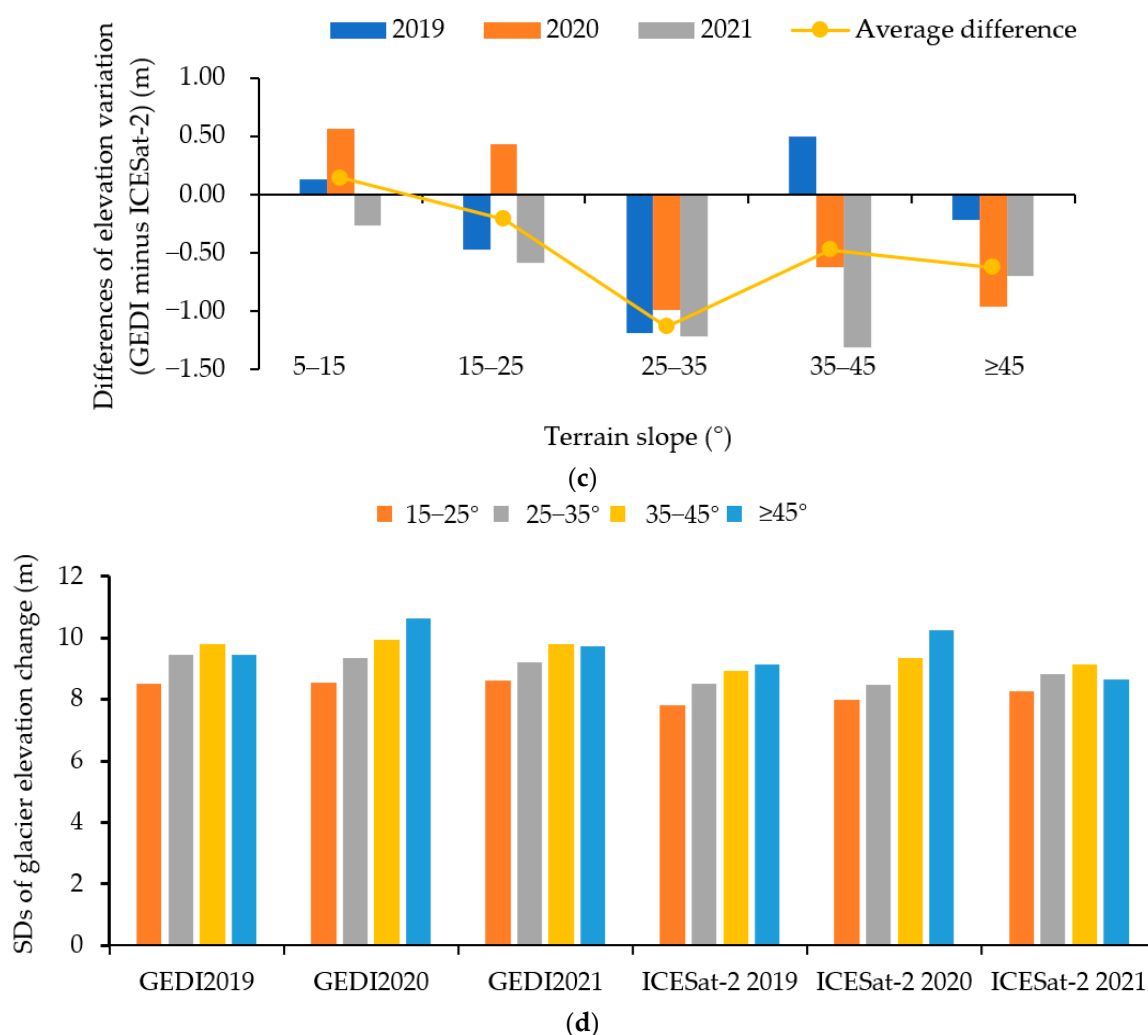
Figure 7. (**a**) Distribution of glacier area and quantity on different slopes; (**b**) comparison of changes in glacier elevation within different terrain slopes derived from GEDI and ICESat-2; (**c**) comparative analysis of elevation differences between GEDI and ICESat-2 at different slope grades; (**d**) standard deviation of elevation changes retrieved using GEDI and ICESat-2 for different slopes.

Figure 7b illustrates the changes in glacier elevation as the slope increases: as the slope increased, the glacier thinning generally showed a trend of first decreasing, then increasing, and then decreasing again. Specifically, the glaciers with the largest thinning were distributed in slope grades less than 5–15°. The thinning gradually decreased in glaciers distributed between 15 and 35°, and a further increase was seen in glaciers distributed between 35 and 45°. When the slope was greater than 45°, the thinning height began to decrease again. Compared to ICESat-2, GEDI showed an overall overestimation of changes in glacier elevation across different slope grades, with the average thinning values of the five slope grades (5–15°, 15–25°, 25–35°, 35–45°, and ≥45°, in turn) being −4.82 m versus −4.96 m, −3.68 m versus −3.47 m, −3.17 m versus −2.04 m, −2.62 m versus −2.14 m, and −2.88 m versus −2.25 m, respectively.

Figure 7c further quantifies the average differences at different slope grades, which demonstrates that the highest absolute difference occurred between 25 and 35° from 2019 to 2021. As the slope increased, the SDs of both elevation changes gradually increased, with average differences of 0.14 m, −0.21 m, −1.13 m, −0.48 m, and −0.63 m. Figure 7d shows that the SDs of GEDI elevation differences ranged from 7.95 to 10.65 m, and the corresponding SDs of ICESat-2 ranged from 6.91 to 10.25 m, indicating that the uncertainty of glacier elevation changes gradually decreased as the slope increased.

(2)　Terrain aspect and Glacier elevation change

Aspect (slope azimuth) influences glacier distribution and changes by affecting solar radiation exposure, altering energy and mass balance. We divided the terrain aspect into eight grades based on the average aspect of each glacier, as shown in Figure 8a: north (N), northeast (NE), east (E), southeast (SE), south (S), southwest (SW), west (W), and northwest (NW). This indicates the uneven distribution of glaciers over the SETP across the eight grades. Using NW and SE as dividing lines, regardless of area or quantity, analysis of slope azimuth reveals significant hemispheric asymmetry in glacier distribution. North-facing slopes (N, NE, E) account for 56.08% of total glacier area and 49.61% of glacier count, whereas south-facing aspects (S, SW, W) account for 22.05% of the total glacier area and 27.23% of glacier area, respectively. This pronounced north–south contrast primarily stems from differential solar radiation receipt, where reduced insolation on northern slopes promotes favorable conditions for ice accumulation and preservation. The observed distribution pattern aligns with established principles of topographic shading's effects on glacier mass balance.
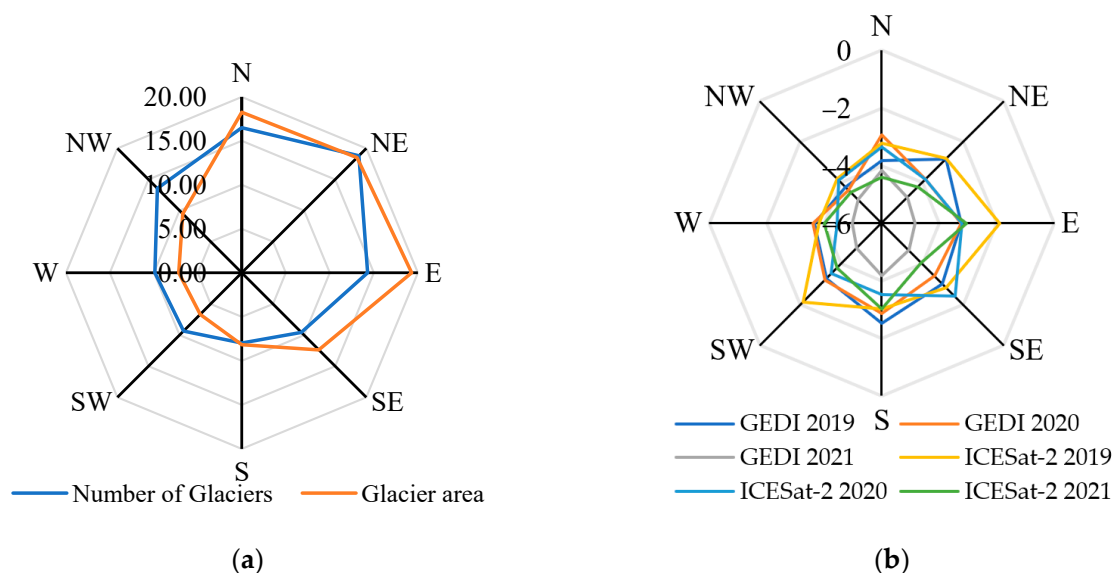

(a)　　　　　　　　　　　　　　　　　　(b)

Figure 8. (a) Distribution of the quantity and area (%) of glaciers within different aspects; (b) cumulative changes in glacier elevation within different aspects derived from GEDI and ICESat-2.

Figure 8b depicts glacier elevation changes in different aspects. Comparing the glacier thinning values identified with GEDI and ICESat-2, it was found that the three slope directions with the largest glacier elevation changes in 2019 were consistently the NW, N, and W slopes. The corresponding change results were -4.21 ± 8.36 m versus 3.8 ± 7.66 m, -3.83 ± 8.44 m versus -3.23 ± 8.25 m, and -3.67 ± 8.73 m versus 3.82 ± 8.25 m. Significant differences were distributed in the E and SW slopes. In 2020, the three directions with significant changes were also consistent, namely the NW (-4.37 ± 8.74 m versus -3.84 ± 7.64 m), W (-3.61 ± 9.07 m versus -4.44 ± 8.25 m), and NE (-3.85 ± 8.61 m vs. -3.89 ± 8.42 m) slopes, with significant differences distributed in the SE direction. The directions with significant changes in 2021 were NW and W, in addition to the E and S slopes. Overall, the three directions with significant changes over the three years analyzed were NW, W, and SW, consistent with glacier distribution and possibly due to the greater solar radiation on the sunny slopes that was not conducive to glacier accumulation.

4.3. Influence of Glacier Attributes on Changes in Elevation

4.3.1. Glacier Areas

We analyzed glacier elevation changes across eight size classes (from <0.1 km² to >10 km²), revealing distinct distribution patterns (Figure 9a). While small glaciers (<0.5 km²) dominated numerically (72.75% of total count, 5225 glaciers), they accounted for less than 1% of the total area. Conversely, only 84 large glaciers (>10 km²) comprised 36.06% of the glacierized area. Most glacier areas (59.11%, 3807.42 km²) were concentrated in mid-size glaciers (0.2–10 km²), with peak abundance occurring at <0.1 km² (2284 glaciers) and 0.2–0.5 km² (1645 glaciers). Unlike previous studies that excluded small glaciers, we intentionally retained all size classes to comprehensively evaluate GEDI's monitoring capabilities across the full glacier-size spectrum.

Both GEDI and ICESat-2 detected consistent thinning across all glacier sizes in the SETP, with distinct area-dependent patterns (Figure 9b). Small glaciers (<0.2 km²) exhibited the most rapid thinning, while mid-sized glaciers (0.2–5 km²) showed gradually reduced thinning rates. This trend reversed for larger glaciers (5–10 km²), followed by a renewed decline in thinning rates for glaciers >10 km². Annually, GEDI overestimated elevation losses compared to ICESat-2 (e.g., −5.34 m vs. −4.73 m in 2021), but both sensors revealed that small glaciers thinned ~3× faster than those >10 km² (e.g., −1.24 m/yr vs. −0.49 m/yr for GEDI).

Discrepancies between GEDI and ICESat-2 were most pronounced for glaciers of 0.5–2 km² (from −0.77 m to −0.54 m differences, Figure 9c). The largest absolute differences occurred for glaciers >10 km², likely due to an uneven data distribution. Despite these variations, both datasets confirmed that smaller glaciers experienced disproportionately higher elevation loss rates, highlighting their heightened vulnerability to climate change.
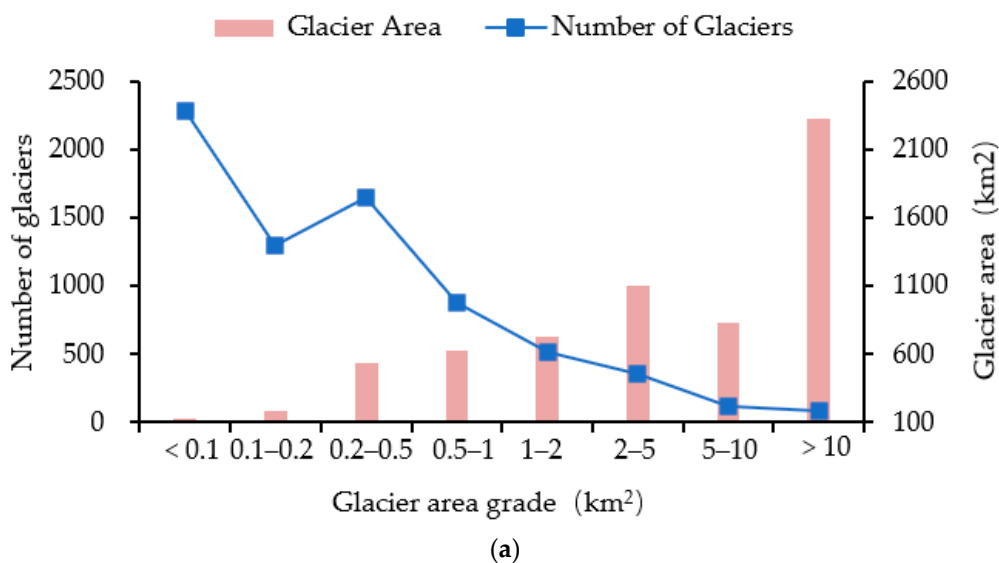

(**a**)
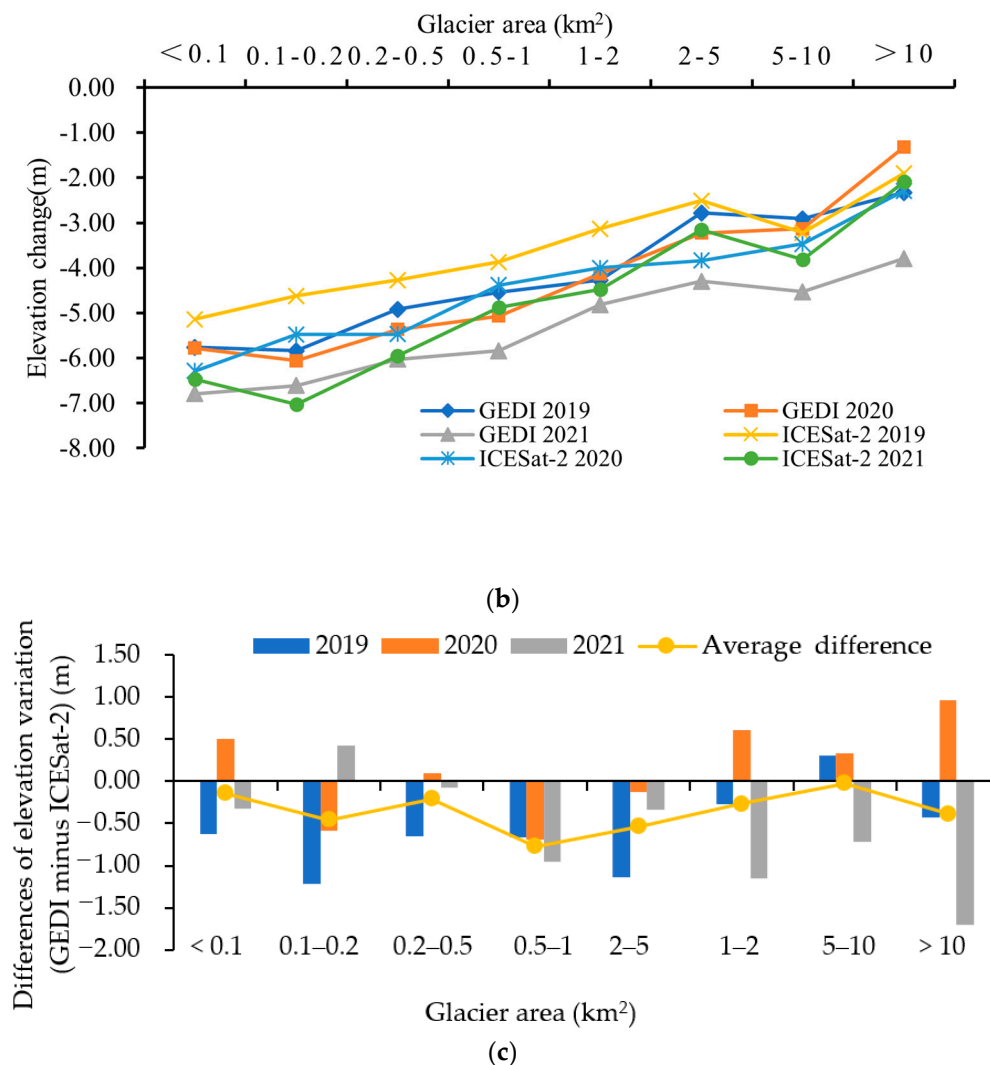
Figure 9. *Cont.*

(b)

(c)

Figure 9. (**a**) Distribution of glacier area grades by quantity and area; (**b**) changes in glacier elevation within different areas derived from GEDI and ICESat-2; (**c**) comparative analysis of differences in elevation between GEDI and ICESat-2 data at different area levels.

4.3.2. Glacier Moraines

Supraglacial debris is a critical factor influencing glacier changes. To investigate the impact of supraglacial debris on glacier elevation changes, glaciers in the SETP were divided into two categories and studied separately according to their distribution: those with a supraglacial debris cover (debris-covered glaciers) and those without (debris-free glaciers). According to statistics on glacier attributes, 348 glaciers had a debris cover and 6834 did not, accounting for 4.85% and 95.15%, respectively. Figure 10 illustrates the elevation changes in the two types of glaciers: debrisflag1 denotes the glaciers with moraines, and debrisflag0 notes the clean glaciers.

The figure clearly shows that, regardless of the type, both glacier groups showed a common thinning trend; however, the changes in debris-covered glaciers were smaller than in those debris-free glaciers, indicating that the supraglacial debris had reached a certain thickness and could effectively reduce the heat absorption capacity of the glacier surface, thus slowing down the melting rate. From 2019 to 2021, the average elevation changes in the two types of glaciers were −2.90 m versus −4.35 m for GEDI and −2.19 m versus −4.27 m for ICESat-2. The average inhibition rates estimated using GEDI and ICESat-2 were 34.11% and 47.80%, respectively, when comparing the melting rate of debris-free

glaciers, illustrating that the supraglacial debris of glaciers has a significant impact on the melting and ice loss of glaciers over the SETP.
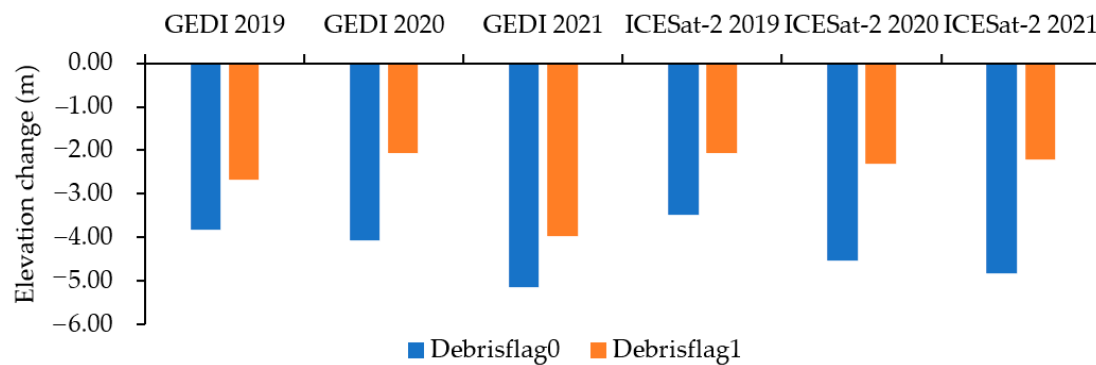

Figure 10. Changes in glacier elevation with and without debris cover derived from GEDI and ICESat-2.

5. Discussion

Given the absence of high-precision field measurements in these extreme glacial environments, we evaluated GEDI-derived elevation changes using comparisons with higher-accuracy ICESat-2 data, focusing on relative trends rather than absolute values. We then contextualize these elevation variations within the existing literature, and examine the key factors affecting monitoring accuracy, including (1) GEDI data quality, (2) ICESat-2 ATL06 product reliability, and (3) TanDEM-X DEM performance.

5.1. Comparison with Similar Surface Elevation Estimates over SETP

Our study compared GEDI and ICESat-2 glacier elevation measurements, quantifying their differences. As GEDI applications in HMA glaciers were previously unexplored, we focused on ICESat-2′s high-precision data for elevation change analysis. GEDI detected an average annual elevation loss of -0.70 ± 0.12 m/yr (2019–2021) in SETP glaciers, consistent with previous findings [6,11].

Using the ASTER optical satellite stereo pairs, Brun et al. [9] found that the Nyainqen-tanglha region had a very negative rate of elevation change: -0.72 ± 0.27 m/yr between 2000 and 2016. Zhao et al. [11] combined multi-satellite altimetry (ICESat, CryoSat-2, ICESat-2), DEM differencing, and gravity data to estimate glacier elevation changes across the SETP. They found an average thinning rate of -0.71 ± 0.18 m/yr (2000–2019) and -0.83 ± 0.04 m/yr (2011–2020). While our sub-regional division aligns with Zhao et al.'s study, slight differences exist due to unclear sub-regional boundaries. Additionally, the study periods differ, which may contribute to variations in the estimated elevation changes. Despite minor numerical variations, the spatial trends agree: Eastern_Bomi showed the fastest thinning, Southern_Yigong the slowest, and Eastern_Yigong's melting rate closely matched the SETP-wide average. Moreover, Shen et al. [31] used ICESat1/2 and SRTM DEM to estimate the interannual and intra-annual elevation changes in glaciers in the entirety of HMA (2003–2020), indicating a faster thinning rate in recent years. Among the sub-regions, the results show that the annual glacier elevation change rate in Nyainqen-tanglha glaciers increased from -0.81 ± 0.15 m/yr in 2003–2008 to -1.12 ± 0.13 m/yr in 2003–2020, which was the region with the fastest glacier loss. Fan et al. [29] determined a glacier thinning rate of -0.81 ± 0.18 m/yr (2003–2021) in the Hengduan Mountains using ICESat-2 and NASADEM data, corroborating the widespread rapid thinning observed across the SETP in previous studies. While our results show slight numerical variations compared to existing research, these differences fall within an acceptable range, and may be attributed to several factors: the uneven spatial distribution of GEDI data, inconsistencies

in data processing methodologies, variations in study periods, and differences in research area boundaries.

At the seasonal scale, our GEDI results reveal clear seasonal glacier elevation patterns, with accumulation predominantly occurring during winter and spring (albeit minimal in spring) and accelerated melting in summer and autumn. These observations are consistent with previous ICESat-2 studies: Shen et al. [31] documented peak glacier elevations in spring and winter-spring thickening in the Nyainqentanglha region (2019–2020), while Wang et al. [30] reported similar winter-spring thickening and summer–autumn thinning patterns across the entire HMA (2018–2020), noting that glacier surfaces typically reach their lowest levels in September–October. Specifically, for Indian monsoon-influenced glaciers in the Nyaingentanglha-Hengduan region, they observed winter thickening (October–March) with distinct altitude-dependent variations, showing slight gains at higher elevations, but significant losses at lower elevations. This strong agreement with independent ICESat-2 findings validates the reliability of GEDI L2A data for glaciological research, particularly in areas where higher-precision altimetry data are scarce. However, temporal mismatches of the two missions could affect results in accumulation zones. Enderlin et al. (2022) [45] showed ICESat-2 season-dependent elevation patterns requiring correction ($\pm$0.5–1.2 m errors if ignored). Therefore, in the future, best practices include hydrological year normalization and snowpack adjustments, which should be adopted in GEDI performance assessment.

5.2. Factors Affecting the Monitoring Accuracy of Changes in Glacier Elevation

(1)   Accuracy of the GEDI altimetric product

In our study, the latest version (2) of GEDI products was used, which improved geolocation compared to version 1. Overall, 95% of the mission weeks had a 1-sigma geolocation error less than 11.9 m. The mean geolocation accuracy was 10.3 m (1 σ offset). The horizontal 10 m offset of the footprint center translates to a corresponding 10 m $\times$ tan (slope) vertical offset. For example, a mean vertical error of about 5 m would be introduced for a 25° slope. Thus, increasing slopes lead to an increasing negative deviation between the glacier estimates of GEDI and the reference counterpart ICESat-2 (Figure 7c). Nevertheless, we applied the parameters 'quality_flag' and 'degrade_flag' to help increase the precision of GEDI elevation estimates by filtering out more outliers. There are still many parameters affecting product accuracy that need to be discussed, such as acquisition time (day or night), beam mode (strong or weak beams), sensitivity, or different denoising algorithms (a1–a6). In addition, it is notable that the distribution of the GEDI footprints is uneven in space and time, which directly affects the measurement accuracy of the height and characteristics of temporal–spatial changes in glacier elevation.

(2)   Accuracy of the ICESat-2 altimetric product and reference DEM data

The accuracy of spaceborne elevation estimates depends heavily on reference data quality. While ICESat-2′s photon-counting technique offers superior resolution (0.7 m photon spacing), its processed ATL06 data averages measurements up to 20 m resolution, with reduced accuracy in steep terrain. Although theoretical vertical errors are <0.1 m on flat ground, real-world performance degrades with increasing slope (Figure 7d) due to geolocation uncertainties from orbital and pointing variations. Additionally, the 91-day revisit cycle creates temporal mismatches with GEDI observations, potentially introducing seasonal surface change artifacts during the gap period.

The TanDEM-X DEM demonstrates a global vertical accuracy of 1.09 m, although this degrades in mountainous regions due to geolocation errors and X-band signal penetration (reaching 4–6 m in dry snow zones) [31]. Compared to ICESat-2′s penetration-free laser altimetry, TanDEM-X systematically underestimates ice elevation by 2.25 $\pm$ 1.68 m on

average in Hengduan Shan [46,47]. Key limitations include (1) multi-year data acquisition (2010–2015), as noted in Section 2.3, introducing temporal uncertainties in the assessment of glacier changes, particularly for dynamic regions with significant interannual variability, (2) uncorrected seasonal penetration variations due to unknown acquisition timing, and (3) resolution mismatches between GEDI's 25 m footprints and TanDEM-X's 12 m pixels. While suitable for studying flat glacier termini, TanDEM-X requires improvements for steep terrain applications. Future studies should employ footprint-averaged DEM values rather than bilinear interpolation and incorporate time-specific validation data to enhance accuracy.

6. Conclusions

Glaciers in HMA are the world's largest storage source of frozen water outside of polar regions and, as such, are an important water source for millions of people. GEDI provides an opportunity to survey changes in glacier surface elevation in unprecedented detail. This study uses the SETP, one of the most sensitive areas to climate change, as the test area in order to assess the performance of GEDI in monitoring glacier elevation changes, with the ICESat-2 high-accuracy land ice ATL06 and reference TanDEM-X DEM products used for comparison. Firstly, the preprocessing of both datasets was implemented using the glacier inventory, and the obvious outliers were deleted using quality metrics provided by the products themselves. Subsequently, we took the TanDEM-X DEM as a reference for past data to estimate the multi-year elevation change; the differences between ICESat-2 and the TanDEM-X DEMs were used as a comparison for the GEDI-based counterpart. Finally, possible affecting factors, such as the terrain features—including altitude, slope, and aspect—and glacier attributes, such as area grade and debris cover, were analyzed to assess GEDI's ability to monitor glacier elevation changes.

The results show that the GEDI elevation values have relatively high outliers in complex mountain glacier areas. According to our method of extracting changes in elevation, the average data retention rate of GEDI from 2019 to 2021 was 29.17%. Compared with ICESat-2, from the perspective of changes in the numerical values of annual glacier elevation, GEDI overestimated glacier elevation melting to some extent with a mean difference bias of −0.29 m, and the corresponding accuracy metrics SD and MAD were larger than those of ICESat-2, with biases of 0.54 m and 0.43 m. However, when comparing the annual glacier thinning rates over the entire SETP, the two are relatively close, with a mean of −0.60 ± 0.19 m/yr versus −0.58 ± 0.15 m/yr and a median of −0.70 ± 0.12 m/yr versus −0.62 ± 0.08 m/yr, respectively.

The corresponding changes in non-glacier areas are also relatively close, indicating that the GEDI data can be used effectively for monitoring mountain glacier elevation changes. In the sub-regions, where glaciers are mainly concentrated, there is a significant difference in the absolute amount of glacier changes, which may be due not only to the quality of the data itself and the terrain factors, but also to the uneven distribution of the GEDI and ICESat-2 data. On a seasonal scale, GEDI reflected the same change trend as ICESat-2, with greater melting occurring in autumn and summer and less melting occurring in spring and winter. Compared to ICESat-2, the elevation variation differences were within a ± 0.8 m range. Nevertheless, the GEDI mission allowed us to capture the monthly, seasonal, and annual dynamics of the changes in glacier surface elevation, and the results indicate that the dataset is a valuable resource for hydrological and climatic change studies.

Moreover, considering terrain factors, the distribution of footprint points in GEDI was uneven at different altitudes, mainly from 4500 m to 6000 m. GEDI revealed similar changing patterns for glacier clusters at different altitudes, slopes, and aspects. Specifically, as the altitude increases, the elevation thinning generally decreases until accumulation

occurs. This change pattern was synchronously influenced by the distribution of glacier area and the effective number of footprints at different altitudes. In addition, the spatial heterogeneity of elevation changes for glacier clusters was strongly controlled by local topographic slope and aspect parameters that modify solar insolation. The distribution of glaciers was mainly concentrated within a slope range of 15–35°, with a gradually decreasing melting rate. As the slope increases, the standard deviation also gradually increases, indicating that the accuracy of GEDI elevation monitoring gradually decreases with an increase in slope. Thus, in future research, terrain slopes can be used as a filter for the dataset when applied to some specific research objectives. Among topographic factors, aspect has a particularly significant impact on glaciers. North-facing slopes favor glacier preservation, leading to higher concentrations, whereas south-facing slopes receive more solar radiation, resulting in greater melt. Generally, the number and spatial distribution of GEDI footprints will directly affect the accuracy of the results. Therefore, to improve the analysis of changes in glacier elevation, the terrain factors should be comprehensively considered when using GEDI or ICESat-2 altimetry data.

In terms of the attributes of the glaciers themselves, GEDI reflected that small glaciers underwent greater changes than large glaciers, and the thinning rate of glaciers with an area less than 0.1 km^2 was about three times that of glaciers with an area greater than 10 km^2, which provides valuable information for monitoring the changes in elevation of small glaciers. Meanwhile, GEDI also revealed that glacier moraines significantly inhibited the melting rate to about 34.11% compared to glaciers without moraines. This indicates that the thickness of glacial moraines has reached a certain level in this area, providing new ideas for slowing down glacier melting.

Overall, our quantitative comparison, assessments, and accuracy analysis of GEDI's multi-beam large-footprint surface elevation observations with those of the higher-accuracy ICESat-2 ATL06 land ice products greatly increase our confidence in using GEDI data for monitoring changes in the elevation of mountain glaciers and aid in understanding their present state and future changes. While GEDI provides valuable large-scale elevation data, its spatial resolution may not capture fine-scale glacial dynamics. In the future, combining these two missions can allow us to take advantage of the strengths of each instrument to extend geographic coverage and increase the sampling density and measurement frequency of mid- and low-latitude mountain glaciers, therefore improving the accuracy of glacier elevation changes and mass balance retrieval.

Conflicts of Interest: The authors declare that they have no known competing financial interests or personal relationships that could have appeared to influence the work reported in this paper.

References

1. Rounce, D.R.; Hock, R.; Maussion, F.; Hugonnet, R.; Kochtitzky, W.; Huss, M.; Berthier, E.; Brinkerhoff, D.; Compagno, L.; Copland, L.; et al. Global glacier change in the 21st century: Every increase in temperature matters. *Science* **2023**, *379*, 78–83. [CrossRef] [PubMed]

2. Wei, Q.; Liu, Y.; Yan, Q.; Yao, T.; Wang, M.; Huang, H.; Hu, Y. The glacier—Climate interaction over the Tibetan Plateau and its surroundings during the Last Glacial Maximum. *Geophys. Res. Lett.* **2013**, *50*, e2023GL103538. [CrossRef]

3. Sakai, A.; Fujita, K. Contrasting glacier responses to recent climate change in high-mountain Asia. *Sci. Rep.* **2017**, *7*, 13717. [CrossRef]

4. Dehecq, A.; Gourmelen, N.; Gardner, A.S.; Brun, F.; Goldberg, D.; Nienow, P.W.; Berthier, E.; Vincent, C.; Wagnon, P.; Trouvé, E. Twenty-first century glacier slowdown driven by mass loss in High Mountain Asia. *Nat. Geosci.* **2019**, *12*, 22–27. [CrossRef]

5. Cauvy-Frauníe, S.; Dangles, O. A global synthesis of biodiversity responses to glacier retreat. *Nat. Ecol. Evol.* **2019**, *3*, 1675–1685. [CrossRef] [PubMed]

6. Hugonnet, R.; McNabb, R.; Berthier, E.; Menounos, B.; Nuth, C.; Girod, L.; Farinotti, D.; Huss, M.; Dussaillant, I.; Brun, F.; et al. Accelerated global glacier mass loss in the early twenty-first century. *Nature* **2021**, *592*, 726–731. [CrossRef]

7. Deng, H.; Chen, Y.; Li, Y. Glacier and snow variations and their impacts on regional water resources in mountains. *J. Geogr. Sci.* **2019**, *29*, 84–100. [CrossRef]

8. Castellazzi, P.; Burgess, D.; Rivera, A.; Huang, J.; Longuevergne, L.; Demuth, M.N. Glacial melt and potential impacts on water resources in the Canadian Rocky Mountains. *Water Resour. Res.* **2019**, *55*, 10191–10217. [CrossRef]

9. Motschmann, A.; Huggel, C.; Carey, M.; Moulton, H.; Walker-Crawford, N.; Muñoz, R. Losses and damages connected to glacier retreat in the Cordillera Blanca, Peru. *Clim. Change* **2020**, *162*, 837–858. [CrossRef]

10. Brun, F.; Berthier, E.; Wagnon, P.; Kääb, A.; Treichler, D. A spatially resolved estimate of High Mountain Asia glacier mass balances from 2000 to 2016. *Nat. Geosci.* **2017**, *10*, 668–673. [CrossRef]

11. Zhao, F.; Long, D.; Li, X.; Huang, Q.; Han, P. Rapid glacier mass loss in the Southeastern Tibetan Plateau since the year 2000 from satellite observations. *Remote Sens. Environ.* **2022**, *270*, 112853. [CrossRef]

12. Guerra-Hernández, J.; Pascual, A. Using GEDI lidar data and airborne laser scanning to assess height growth dynamics in fast-growing species: A showcase in Spain. *For. Ecosyst.* **2021**, *8*, 14. [CrossRef]

13. Trantow, T.; Herzfeld, U.C. Spatiotemporal mapping of a large mountain glacier from CryoSat-2 altimeter data: Surface elevation and elevation change of Bering Glacier during surge (2011–2014). *Int. J. Remote Sens.* **2016**, *37*, 2962–2989. [CrossRef]

14. Shean, D.E.; Bhushan, S.; Montesano, P.; Rounce, D.R.; Arendt, A.; Osmanoglu, B. A systematic, regional assessment of high mountain Asia glacier mass balance. *Front. Earth Sci.* **2020**, *7*, 363. [CrossRef]

15. Brown, M.E.; Arias, S.D.; Chesnes, M. Review of ICESat and ICESat-2 literature to enhance applications discovery. *Remote Sens. Appl. Soc. Environ.* **2023**, *29*, 100874. [CrossRef]

16. Markus, T.; Neumann, T.; Martino, A.; Abdalati, W.; Brunt, K.; Csatho, B.; Farrell, S.; Fricker, H.; Gardner, A.; Harding, D.; et al. The Ice, Cloud, and Land Elevation Satellite-2 (ICESat-2): Science requirements, concept, and implementation. *Remote Sens. Environ.* **2017**, *190*, 260–273. [CrossRef]

17. Dubayah, R.; Goetz, S.J.; Blair, J.B.; Fatoyinbo, T.E.; Hansen, M.; Healey, S.P.; Hofton, M.A.; Hurtt, G.C.; Kellner, J.; Luthcke, S.B.; et al. The Global Ecosystem Dynamics Investigation: High-resolution laser ranging of the Earth's forests and topography. *Sci. Remote Sens.* **2020**, *1*, 100002. [CrossRef]

18. Potapov, P.; Li, X.; Hernandez-Serna, A.; Tyukavina, A.; Hansen, M.C.; Kommareddy, A.; Pickens, A.; Turubanova, S.; Tang, H.; Silva, C.E.; et al. Mapping global forest canopy height through integration of GEDI and Landsat data. *Remote Sens. Environ.* **2021**, *253*, 112165. [CrossRef]

19. Simard, M.; Pinto, N.; Fisher, J.B.; Baccini, A. Mapping forest canopy height globally with spaceborne lidar. *J. Geophys. Res. Biogeosci.* **2011**, *116*, G04021. [CrossRef]

20. Schneider, F.D.; Ferraz, A.; Hancock, S.; Duncanson, L.I.; Dubayah, R.O.; Pavlick, R.P.; Schimel, D.S. Towards mapping the diversity of canopy structure from space with GEDI. *Environ. Res. Lett.* **2020**, *15*, 115006. [CrossRef]

21. Marselis, S.M.; Abernethy, K.; Alonso, A.; Armston, J.; Baker, T.R.; Bastin, J.; Bogaert, J.; Boyd, D.S.; Boeckx, P.; Burslem, D.F.R.P.; et al. Evaluating the potential of full-waveform lidar for mapping pan-tropical tree species richness. *Glob. Ecol. Biogeogr.* **2020**, *29*, 1799–1816. [CrossRef]

22. Adam, M.; Urbazaev, M.; Dubois, C.; Schmullius, C. Accuracy assessment of GEDI terrain elevation and canopy height estimates in European temperate forests: Influence of environmental and acquisition parameters. *Remote Sens.* **2020**, *12*, 3948. [CrossRef]

23. Kutchartt, E.; Pedron, M.; Pirotti, F. Assessment of canopy and ground height accuracy from GEDI lidar over steep mountain areas. *ISPRS Ann. Photogramm. Remote Sens. Spat. Inf. Sci.* **2022**, *3*, 431–438. [CrossRef]

24. Quiros, E.; Polo, M.-E.; Fragoso-Campon, L. GEDI elevation accuracy assessment: A case study of southwest Spain. *IEEE J. Sel. Top. Appl. Earth Obs. Remote Sens.* **2021**, *14*, 5285–5299. [CrossRef]

25. Hamoudzadeh, A.; Ravanelli, R.; Crespi, M. Glacier monitoring using GEDI data in Google Earth Engine: Outlier removal and accuracy assessment. In *EGU General Assembly Conference Abstracts*; European Geosciences Union: Munich, Germany, 2024; p. 10176.

26. Besso, H.; Shean, D.; Lundquist, J.D. Mountain snow depth retrievals from customized processing of ICESat-2 satellite laser altimetry. *Remote Sens. Environ.* **2024**, *300*, 113843. [CrossRef]

27. Koo, Y.H.; Xie, N.T.; Kurtz, S.F.; Ackley, W.; Wang, W. Sea ice surface type classification of ICESat-2 ATL07 data by using data-driven machine learning model: Ross Sea, Antarctic as an example. *Remote Sens. Environ.* **2023**, *296*, 113726. [CrossRef]

28. Xu, X.; Wang, W.; Huang, D.; Hu, X.; Fu, W. Assessment of interannual and seasonal glacier mass changes in the Karakoram during 2018–2022 using ICESat-2 data. *J. Hydrol.* **2023**, *626*, 130223. [CrossRef]

29. Fan, Y.; Ke, C.-Q.; Zhou, X.; Shen, X.; Yu, X.; Lhakpa, D. Glacier mass-balance estimates over High Mountain Asia from 2000 to 2021 based on ICESat-2 and NASADEM. *J. Glaciol.* **2023**, *69*, 500–512. [CrossRef]

30. Wang, Q.; Sun, W. Seasonal cycles of high mountain Asia glacier surface elevation detected by ICESat-2. *J. Geophys. Res. Atmos.* **2022**, *127*, e2022JD037501. [CrossRef]

31. Shen, C.; Jia, L.; Ren, S. Inter- and intra-annual glacier elevation change in high mountain Asia region based on ICESat-1&2 data using elevation-aspect bin analysis method. *Remote Sens.* **2022**, *14*, 1630. [CrossRef]

32. Chen, W.; Yao, T.; Zhang, G.; Li, F.; Zheng, G.; Zhou, Y.; Xu, F. Towards ice-thickness inversion: An evaluation of global digital elevation models (DEMs) in the glacierized Tibetan Plateau. *Cryosphere* **2021**, *16*, 197–218. [CrossRef]

33. Wang, Q.; Yi, S.; Sun, W. Continuous estimates of glacier mass balance in high mountain Asia based on ICESat-1, 2 and GRACE/GRACE follow-on data. *Geophys. Res. Lett.* **2021**, *48*, e2020GL090954. [CrossRef]

34. Li, R.; Li, H.; Hao, T.; Qiao, G.; Cui, H.; He, Y.; Hai, G.; Xie, H.; Cheng, Y.; Li, B. Assessment of ICESat-2 ice surface elevations over the Chinese Antarctic Research Expedition (CHINARE) route, East Antarctica, based on coordinated multi-sensor observations. *Cryosphere* **2021**, *15*, 3083–3099. [CrossRef]

35. Zhang, Y.; Pang, Y.; Cui, D.; Ma, Y.; Chen, L. Accuracy assessment of the ICESat-2/ATL06 product in the Qilian mountains based on CORS and UAV data. *IEEE J. Sel. Top. Appl. Earth Obs. Remote Sens.* **2020**, *14*, 1558–1571. [CrossRef]

36. Liu, A.; Cheng, X.; Chen, Z. Performance evaluation of GEDI and ICESat-2 laser altimeter data for terrain and canopy height retrievals. *Remote Sens. Environ.* **2021**, *264*, 112571. [CrossRef]

37. Urbazaev, M.; Hess, L.L.; Hancock, S.; Sato, L.Y.; Ometto, J.P.; Thiel, C.; Dubois, C.; Heckel, K.; Urban, M.; Adam, M.; et al. Assessment of terrain elevation estimates from ICESat-2 and GEDI spaceborne LiDAR missions across different land cover and forest types. *Sci. Remote Sens.* **2022**, *6*, 100067. [CrossRef]

38. Lutz, A.F.; Immerzeel, W.W.; Shrestha, A.B.; Bierkens, M.F.P. Consistent increase in High Asia's runoff due to increasing glacier melt and precipitation. *Nat. Clim. Change* **2014**, *4*, 587–592. [CrossRef]

39. Ke, L.; Ding, X.; Zhang, L.; Hu, J.; Shum, C.K.; Lu, Z. Compiling a new glacier inventory for southeastern Qinghai–Tibet Plateau from Landsat and Palsar data. *J. Glaciol.* **2016**, *62*, 579–592. [CrossRef]

40. Zhang, Y.; Kang, S.; Cong, Z.; Schmale, J.; Liu, Y. Glacier changes and climate trends in the Parlung Zangbo Basin. *Remote Sens.* **2021**, *13*, 891.

41. Brautigam, B.; Gonzalez, J.H.; Schwerdt, M.; Bachmann, M. TerraSAR-X instrument calibration results and extension for TanDEM-X. *IEEE Trans. Geosci. Remote Sens.* **2010**, *48*, 702–715. [CrossRef]

42. Rizzoli, P.; Martone, M.; Gonzalez, C.; Wecklich, C.; Tridon, D.B.; Bräutigam, B.; Bachmann, M.; Schulze, D.; Fritz, T.; Huber, M.; et al. Generation and performance assessment of the global TanDEM-X digital elevation model. *ISPRS J. Photogramm. Remote Sens.* **2017**, *132*, 119–139. [CrossRef]

43. Breit, H.; Younis, M.; Balss, U.; Niedermeier, A.; Grigorov, C.; Hueso-Gonzalez, J.; Krieger, G.; Eineder, M.; Fritz, T. Bistatic synchronization and processing of TanDEM-X data. In Proceedings of the 2011 IEEE International Geoscience and Remote Sensing Symposium, Vancouver, BC, Canada, 24–29 July 2011.

44. Beck, J.; Armston, J.; Hofton, M.; Luthcke, S.J.S.F. *Global Ecosystem Dynamics Investigation (GEDI) Level 02 User Guide*; USGS Earth Resources Observation and Science (EROS) Center: Sioux Falls, SD, USA, 2021.

45. Enderlin, E.M.; Elkin, C.M.; Gendreau, M.; Marshall, H.P.; O'Neel, S.; McNeil, C.; Florentine, C.; Sass, L. Uncertainty of ICESat-2 ATL06- and ATL08-derived snow depths for glacierized and vegetated mountain regions. *Remote Sens. Environ.* **2022**, *283*, 113307. [CrossRef]

46. Dehecq, A.; Millan, R.; Berthier, E.; Gourmelen, N.; Trouvé, E.; Vionnet, V. Elevation changes inferred from TanDEM-X data over the Mont-Blanc area: Impact of the X-band interferometric bias. *IEEE J. Sel. Top. Appl. Earth Obs. Remote Sens.* **2016**, *9*, 3870–3882. [CrossRef]

47. Jaber, W.A.; Rott, H.; Floricioiu, D.; Wuite, J.; Miranda, N. Heterogeneous spatial and temporal pattern of surface elevation change and mass balance of the Patagonian ice fields between 2000 and 2016. *Cryosphere* **2019**, *13*, 2511–2535. [CrossRef]